

Supporting Information

High Thermally Stable n-type Semiconductor up to 850 K based on Dianionic Naphthalenediimide Derivative

Ayumi Kawasaki, Takashi Takeda, Norihisa Hoshino, Wakana Matsuda, Shu Seki, and Tomoyuki Akutagawa

E-mail: akutagawa@tohoku.ac.jp

Contents

1. Experimental Section
2. Molecular orbital DFT calculations of LUMO for dianion and neutral **4** (Figure S1).
3. CV charts of molecules **1**, **2**, and **4** in DMF vs. Ag/AgCl reference electrode (Figure S2).
4. IR spectra of crystals **1** – **4** on KBr pellets (Figure S3)
5. Molecular structure and atomic numbering scheme of molecules **1**, **2**, and **3** based on the single crystal X-ray structural analysis (Figure S4).
6. Unit cells of crystal **2** viewed along the *a* and *c* axis (Figure S5).
7. Unit cells of crystal **3** viewed along the *a* and *b* axis (Figure S6).
8. Temperature and frequency dependent real and imaginary parts of dielectric constants (ϵ_1 and ϵ_2) for pellet of unhydrated crystal **1'** (Figure S7).
9. Temperature and frequency dependent real and imaginary parts of dielectric constants (ϵ_1 and ϵ_2) for pellet of crystal **2** (Figure S8).
10. Temperature and frequency dependent real and imaginary parts of dielectric constants (ϵ_1 and ϵ_2) for pellet of crystal **3** (Figure S9).

11. Temperature and frequency dependent real and imaginary parts of dielectric constants (ϵ_1 and ϵ_2) for pellet of crystal **4** (Figure S10).
12. Proton conductivity of crystal **3** with temperature dependent Cole-Cole plots and proton transport layer (Figure S11).
13. Temperature dependent ionic conductivities of crystals **1**, **2**, and **3** (Figure S12).
14. TAS spectra of thin films **1** – **4** (Figure S13).
15. PXRD patterns of powder **1'**, thin film **1'**, and the simulation of **1** based on the single crystal X-ray analysis (Figure S14).
16. PXRD patterns of powder **2**, thin film **2**, and the simulation of **2** based on the single crystal X-ray analysis (Figure S15).
17. PXRD patterns of powder **3**, thin film **3**, and the simulation of **3** based on the single crystal X-ray analysis (Figure S16).
18. PXRD patterns of powder **4**, thin film **4**, and the simulation of **4** based on the single crystal X-ray analysis (Figure S17).
- 19.** AFM images of thin films a) **1**, b) **2**, and c) **3** for the scanning range of 25 x 25 μm^2 (upper) and 1 x 1 μm^2 (lower) (Figure S18).

1. Experimental Section

General. Ultraviolet/visible/near infrared (UV–vis–NIR) spectra (200–3000 nm) and infrared (IR) spectra (400–4000 cm^{-1}) were obtained for the samples in solution and on KBr pellets and were measured using PerkinElmer Lambda 750 and Thermo Fisher Scientific Nicolet 6700 FT-IR spectrophotometers, respectively. Redox potentials were measured for 0.1 mM solutions of the samples dissolved in anhydrous dimethylformamide (DMF). 0.1 M $n\text{-Bu}_4\text{N}^+\text{BF}_4^-$ was used as the supporting electrolyte; platinum wire was used as the working and counter electrodes; and Ag/AgCl was used as the reference electrode. The redox potentials were scanned at 50 mV s^{-1} and were calibrated using the half-wave oxidation potential of Fc/Fc^+ (0.554 V). Thermogravimetric (TG) and differential thermal (DT) analyses were performed using a Rigaku Thermo Plus TG8120 thermal analysis station and an Al_2O_3 reference. The samples were heated in the range 293–600 K at 5 K min^{-1} under nitrogen.

Preparations of crystals 1, 2, and 3. Sodium sulphonyl acid hydrate (9.76 g, 49.5 mmol) and 1,4,5,8-naphthalene dicarboxylic acid dihydrate (2.29 g, 8.556 mmol) were dissolved in DMF (60 mL) and were refluxed at 135 $^{\circ}\text{C}$ overnight under a N_2 flow. The reaction mixture was then cooled to room temperature, and diethyl ether (80 mL) was added. A precipitate was collected and dried under vacuum. The resultant dark brown powder was recrystallised from water to obtain a yellow–brown powder (**1**) (4.08 mg) with a yield of 77%. ^1H NMR (400 MHz, $\text{DMSO-}d_6$) δ = 8.73 (s, 4H), 8.06 (d, J = 8.5 Hz, 4H), 7.61 (d, J = 8.4 Hz, 4H); IR (KBr, cm^{-1}): 3608 (m), 3500 (s), 3097 (w), 3076 (w), 3064 (w), 1720 (s), 1672 (s), 1583 (s), 1497 (m), 1448 (m), 1402 (m), 1356 (s), 1253 (s), 1201 (s); Anal. Calc. for $\text{C}_{26}\text{H}_{12}\text{N}_2\text{O}_{10}\text{S}_2\text{Na}_2$ C 50.17, H 1.94, N 4.50; Found C 49.88, H 2.19, N 4.50.

Ammonium bromide (2.18 g, 22.7 mmol) was stirred into an aqueous solution of **1** (0.65 g, 1.05 mmol) dissolved in water (80 mL). A precipitate was collected and dried under vacuum. The crude product was recrystallised twice from a water–ethanol mixed solvent (v:v = 1:1), resulting in a yellow powder (**2**) (0.252 g) with a yield of 39%. ^1H NMR (400 MHz, $\text{DMSO-}d_6$) δ = 8.73 (s, 4H),

7.76 (d, $J = 8.5$ Hz, 4H), 7.411 (d, $J = 8.5$ Hz, 4H), 7.08 (t, $J = 50.1$ Hz, 2.8H); IR (KBr, cm^{-1}): 3453 (m), 3176 (s), 3082 (s), 2875 (w), 1715 (s), 1672 (s), 1583 (s), 1515 (w), 1496 (m), 1447 (s), 1403 (s), 1351 (s), 1252 (s), 1227 (s), 1189 (s); Anal. Calc. for $\text{C}_{26}\text{H}_{20}\text{N}_4\text{O}_{10}\text{S}_2$ C 50.98, H 3.29, N 9.15; Found C 50.73, H 3.57, N 9.10.

Tetrabutylammonium bromide (2.96 g, 9.19 mmol) was stirred into an aqueous solution of **1** (2.88 g, 4.62 mmol) dissolved in H_2O (300 mL). Then, CH_2Cl_2 (300 mL) was added into aqueous solution and an organic layer was extracted and washed by H_2O and dried by Na_2SO_4 . A removal of solvent provided the yellow coloured product of $(\text{TBA})_2(\text{BS-NDI}^{2-})$ (3.22 g) with a yield of 66%. ^1H NMR (400 MHz, DMSO) δ 8.73(s, 4H, naphthalenyl H), 7.76 (d, $J = 8.5$ Hz, 4H, phenyl H), 7.41 (d, $J = 8.5$ Hz, 4H, phenyl H), 3.16 (m, 16H), 1.56 (m, 16H), 1.30 (m, 16H), 0.94 (t, $J = 14.8$ Hz, 24H) ppm.

KPF_6 (0.16 g, 0.90 mmol) and $(\text{TBA})_2(\text{BS-NDI}^{2-})$ (0.300g, 0.285 mmol) was stirred in CH_3CN (10 mL), resulting in pink-coloured precipitate, which was filtrated and dried by vacuum. The crude product was recrystallised twice from a water–ethanol mixed solvent (v:v = 1:1), resulting in a orange-coloured crystals (**3**) (0.109 g, 0.166 mmol) with a yield of 58%. ^1H NMR (400 MHz, D_2O): δ 8.81 (4H, s, naphthalene H), 8.03 (4H, d, $J = 8.7$ Hz, phenyl H), 7.58 (4H, d, $J = 8.7$ Hz, phenyl H); IR(KBr, cm^{-1}): 1720, 1676, 1579, 1498, 1446, 1408, 1354, 1252, 1217, 1198, 1144, 1121, 1041, 1018, 980; Elemental Analysis Calc. for $\text{C}_{26}\text{H}_{12}\text{N}_2\text{K}_2\text{O}_{10}\text{S}_2$; C, 47.70; H, 1.85; N, 4.28; Found C, 47.46; H, 1.90; N, 4.30.

Crystal structure characterisations. Single crystals were obtained by slowly evaporating the crystallisation solvents. Crystallographic data were collected using a Rigaku RAPID-II diffractometer equipped with a rotating anode fitted with a multilayer confocal optic and using Cu-K α ($\lambda = 1.54187$ Å) radiation from a graphite monochromator. Structural refinements were performed using the full-matrix least-squares method on F^2 . Calculations were performed using Crystal Structure software packages.^{1,2} All the parameters, except for those of the hydrogen atoms, were refined using anisotropic temperature factors.

Table S1. Crystal Data, Data Collection, and Reduction Parameters.

| | 1•2(H₂O) | 2 | 3 |
|--|--|--|---|
| <i>Chemical formula</i> | C ₂₂ H ₆ N ₄ O ₁₂ S ₂ Na ₂ | C ₂₆ H ₁₂ K ₂ N ₂ O ₁₀ S ₂ | C ₂₆ H ₂₀ N ₄ O ₁₀ S ₂ |
| <i>Formula weight</i> | 658.52 | 654.70 | 612.58 |
| <i>Space group</i> | <i>P</i> 2 ₁ /c (#14) | <i>P</i> 2 ₁ /c (#14) | <i>P</i> -1 (#2) |
| <i>a</i> , Å | 21.0005(8) | 5.37714(10) | 7.39936(19) |
| <i>b</i> , Å | 8.10823(8) | 29.5528(5) | 8.9486(2) |
| <i>c</i> , Å | 7.57570(8) | 7.78118(14) | 20.4815(6) |
| <i>α</i> , deg | - | - | 78.417(2) |
| <i>β</i> , deg | 97.5160(10) | 94.0057(9) | 77.9681(18) |
| <i>γ</i> , deg | - | - | 76.6033(18) |
| <i>V</i> , Å ³ | 1278.8885(4) | 1233.48(4) | 1273.60(6) |
| <i>Z</i> | 2 | 2 | 2 |
| <i>T</i> , K | 100 | 100 | 100 |
| <i>D</i> _{calc} , g·cm ⁻³ | 1.710 | 1.763 | 1.597 |
| <i>μ</i> , cm ⁻¹ | 29.03 | 55.95 | 25.18 |
| <i>Reflections measured</i> | 13855 | 12737 | 14682 |
| <i>Independent reflections</i> | 2346 | 2225 | 4581 |
| <i>Reflections used</i> | 2346 | 2225 | 4581 |
| <i>R</i> _{int} | 0.0550 | 0.1311 | 0.0336 |
| <i>R</i> ₁ ^a | 0.0437 | 0.1108 | 0.0369 |
| <i>R</i> _w (<i>F</i> ₂) ^a | 0.1452 | 0.2269 | 0.1103 |
| <i>GOF</i> | 1.081 | 1.178 | 1.189 |

^a $R_1 = \Sigma ||F_o| - |F_c|| / \Sigma |F_o|$ and $R_w = (\Sigma \omega(|F_o| - |F_c|)^2 / \Sigma \omega F_o^2)^{1/2}$.

Flash-photolysis time-resolved microwave conductivity measurements. Thin films of crystals **1**, **2**, **3**, and **4** were fabricated by drop-casting their aqueous solutions onto quartz substrates ($9 \times 40 \text{ mm}^2 \times 1 \text{ mm}$ thick), which were then dried under vacuum ($< 2 \times 10^{-1} \text{ Pa}$) for 1 h to remove any residual water and subsequently annealed at 120°C . Charge carrier mobilities were evaluated by flash-photolysis time-resolved microwave conductivity (FP-TRMC) under Ar-saturation conditions at 290 K .^{3, 4} Charge carriers were injected into the materials via photoionisation with third-harmonic-generating ($\lambda = 355 \text{ nm}$) Nd:YAG laser (Spectra Physics model INDI-HG) pulses at 10 Hz at ca. 5 ns pulse^{-1} . The photon density of a 355 nm pulse was modulated in the range $4.8\text{--}6.1 \times 10^{15} \text{ photons cm}^{-2} \text{ pulse}^{-1}$. The microwave frequency and power were set at $\sim 9.1 \text{ GHz}$ and 3 mW , respectively, and were guided into a microwave cavity. The Q -factors of the microwave cavity loaded with the samples were 1900 and 2200 at 470 and 290 K , respectively, and the film-coated substrates were set at the maximum electric field. The reflected power of the probing microwave, picked up by a diode (rise time $< 1 \text{ ns}$), was amplified by a Ciao Electronics CA812-304 FET amplifier and was subsequently monitored by a Tektronix model TDS3032B digital oscilloscope. The observed change in the reflected microwave power (ΔP_r) was normalised with the steady reflection of the microwave from the cavity (P_r) and was directly converted into the product of a photocarrier generation yield (ϕ) and the sum of photogenerated electron/hole mobilities ($\Sigma\mu$):

$$\phi\Sigma\mu = 1/(eI_0F_{\text{light}}) \times (1/A) \times (\Delta P_r/P_r), \quad (1)$$

where ε , A , I_0 , and F_{light} are elementary charge, sensitivity factor ($\text{S}^{-1} \text{ cm}$), incident photon density of the excitation laser (photons cm^{-2}), and filling factor (cm^{-1}), respectively. F_{light} was calculated based on the overlap between the photocarrier injection area (presumed to be proportional to the excitation light absorbed by the sample film) and the electric field strength distribution in the cavity, as derived from a calculation code of CST Microwave Studio (AET Inc.).

Transient absorption spectroscopy measurements. To determine the values of ϕ , transient absorption spectroscopy (TAS) was conducted at 290 K for polycrystalline films of crystals **1** and **2** drop-cast onto quartz substrates identical to those used for the FP-TRMC measurements. The optical transmittances of the films were measured for various excitation light pulses, using an Ophir VEGA power meter equipped with a PE25-C sensor head (Newport Corp.) Changes in the time-dependent absorption spectra were measured as two-dimensional images by a Hamamatsu C7700 streak camera via a Hamamatsu C5094 spectrometer upon direct excitation of the films by pulses from the laser system identical to the one used for the FP-TRMC measurements. The excitation density was tuned at $3.2 \times 10^{16} \text{ cm}^{-2} \text{ photons pulse}^{-1}$. The transients were monitored at 480-500 nm where the molar extinction coefficient of $\text{NDI}^{\bullet-}$ was $26000 \text{ M}^{-1} \text{ cm}^{-1}$.⁵ The streak images were averaged typically over 400 scans to correct 2D time–wavelength correlation data of the transient absorption of each film.

Theoretical calculations. The LUMOs of molecules BSNDI^{2-} and **3** were calculated with density functional theory (DFT) using the B3LYP/6-31+G(*d*, *p*) basis set (Gaussian 09).⁶ Atomic coordinates based on the X-ray structural analyses of crystals **1** and **2** were used for single-point energy calculations. The transfer integrals (*t*) between the LUMOs of BSNDI^{2-} in crystals **1** and **2** were calculated within the tight-binding approximation, using the extended Hückel molecular orbital method, where the LUMOs of protonated **H2BSNDI** were used as the basis functions.⁷ Semi-empirical parameters for Slater-type atomic orbitals were obtained from the literature.⁷ The *t* values for each pair of molecules were assumed to be proportional to the overlap integral (*S*) according to the equation $t = -10S \text{ (eV)}$.

References

- (1) Crystal Structure: Single crystal structure analysis software. Ver. 3.6, 2004. Rigaku Corporation and Molecular Structure Corporation.
- (2) Sheldrick, G. M. SHELX97 Programs for Crystal Structure Analysis; Universitat Göttingen: Göttingen, Germany, 1998.
- (3) Seki, S.; Saeki, A.; Sakurai, T.; Sakamaki, D. *Phys. Chem. Chem. Phys.* **2014**, *16*, 11093–11113.
- (4) Tsutsui, Y.; Schweicher, G.; Chattopadhyay, B.; Sakurai, T.; Arlin, J.-B.; Ruzié, C.; Aliev, A.; Ciesielski, A.; Colella, S.; Kennedy, A. R.; Lemaire, V.; Olivier, Y.; Hadji, R.; Sanguinet, L.; Castet, F.; Beljonne, D.; Cornil, J.; Samorì, P.; Seki, S.; Geerts, Y. H. *Adv. Mater.* **2016**, *28*, 7106–7114.
- (5) Gosztola, D.; Niemczyk M. P.; Aaron S.; Lukas W. S.; Wasielewski M. R. *J. Phys. Chem. A* **2000**, *104*, 6545–6551.
- (6) Gaussian 09, Revision C 01: Frisch, M. J.; Trucks, G. W.; Schlegel, H. B.; Scuseria, G. E.; Robb, M. A.; Cheeseman, J. R.; Scalmani, G.; Barone, V.; Mennucci, B.; Petersson, G. A.; et al Gaussian, Inc.: Wallingford, CT, 2009.
- (7) Mori, T.; Kobayashi, A.; Sasaki, Y.; Kobayashi, H.; Saito, G.; Inokuchi, H. *Bull. Chem. Soc. Jpn.* **1984**, *57*, 627–633.

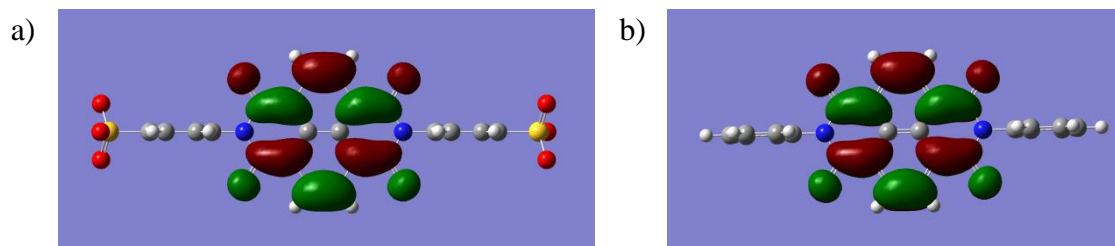


Figure S1. The lowest occupied molecular orbitals (LUMOs) of molecules a) **BSNDI²⁻** and b) *N,N'*-diphenyl-NDI (**4**) calculated with density functional theory (DFT) using the B3LYP/6-31+G(*d*, *p*) basis set (Gaussian 09).

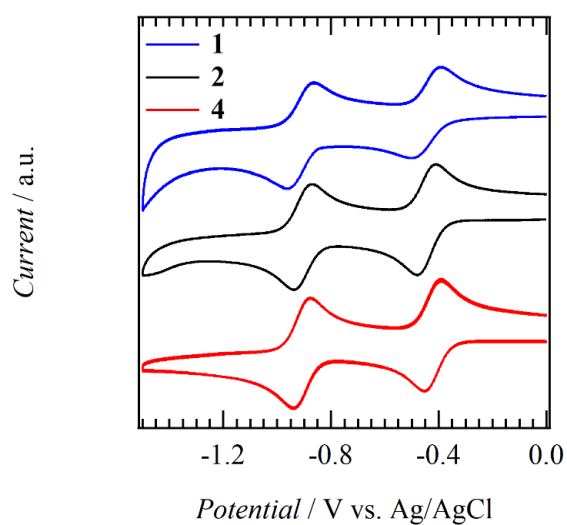


Figure S2. The two-steps reversible half-wave reduction potentials ($E_{1/2}^1$ and $E_{1/2}^2$) of molecules **1**, **2**, and **4** vs. Ag/AgCl reference electrode in DMF. Low solubility of salt **3** in DMF was difficult to measure the CV chart.

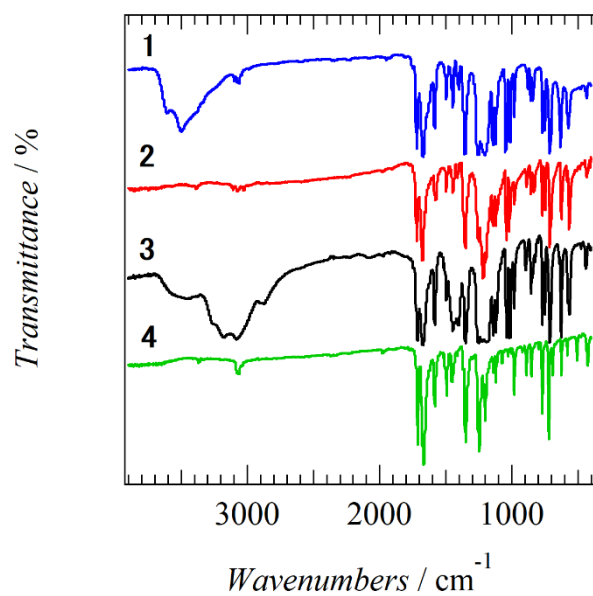


Figure S3. IR spectra of crystals **1** – **4** on KBr pellets

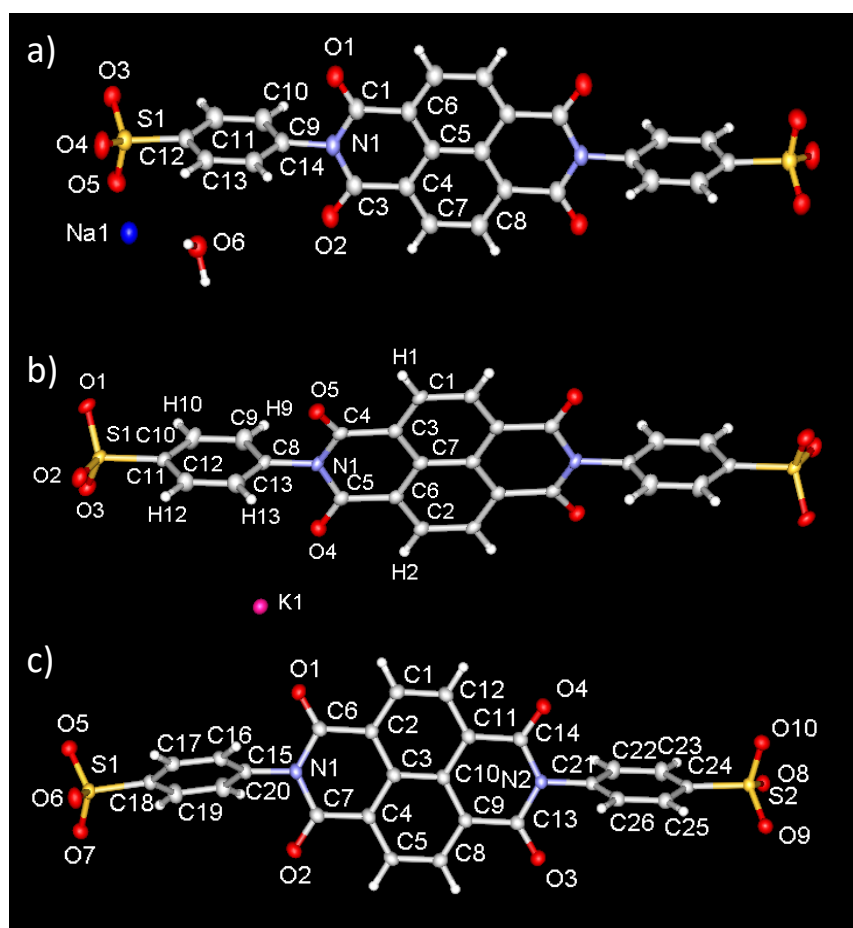


Figure S4. Molecular structure and atomic numbering scheme of molecules **1**, **2**, and **3** based on the single crystal X-ray structural analysis.

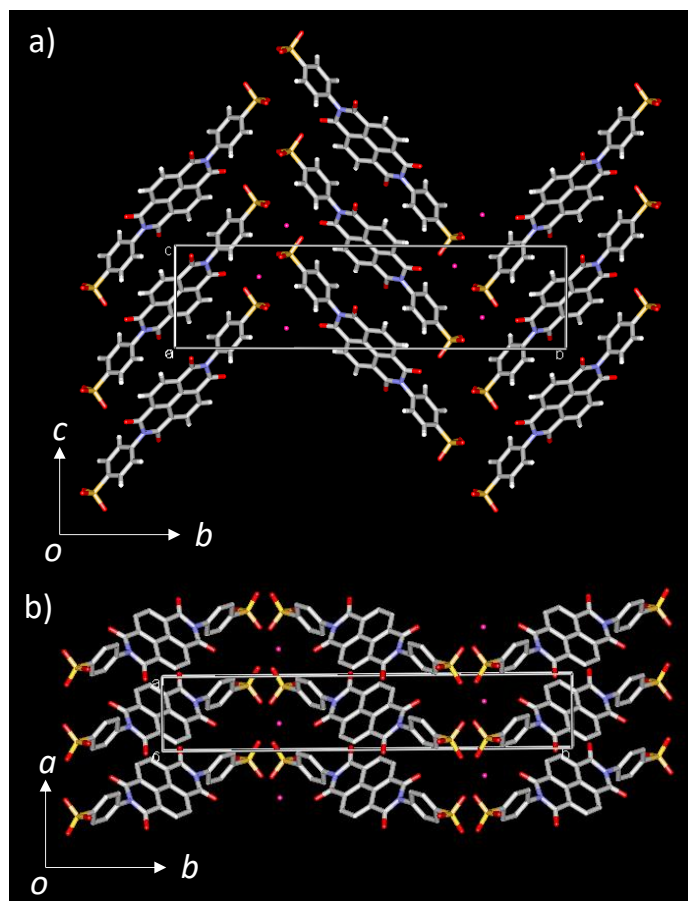


Figure S5. Unit cells of crystal **2** viewed along the *a* and *c* axis.

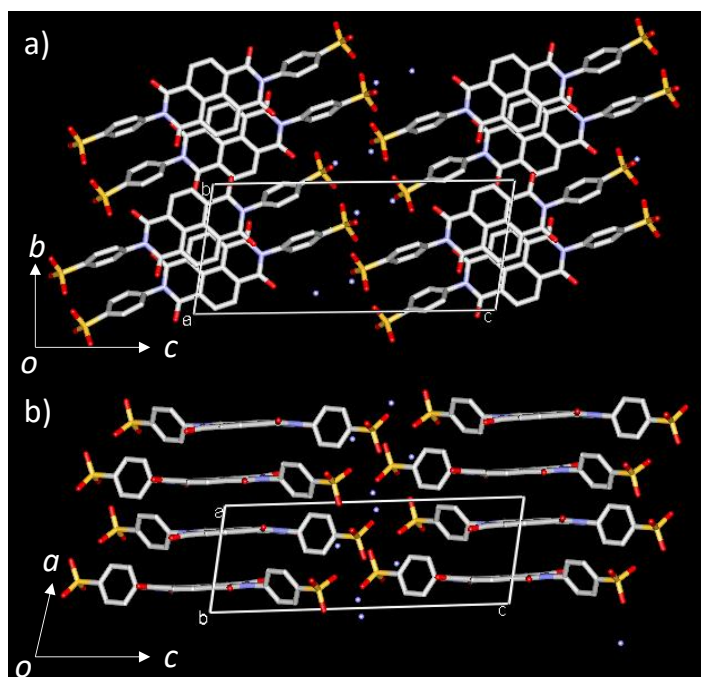


Figure S6. Unit cells of crystal **3** viewed along the *a* and *b* axis.

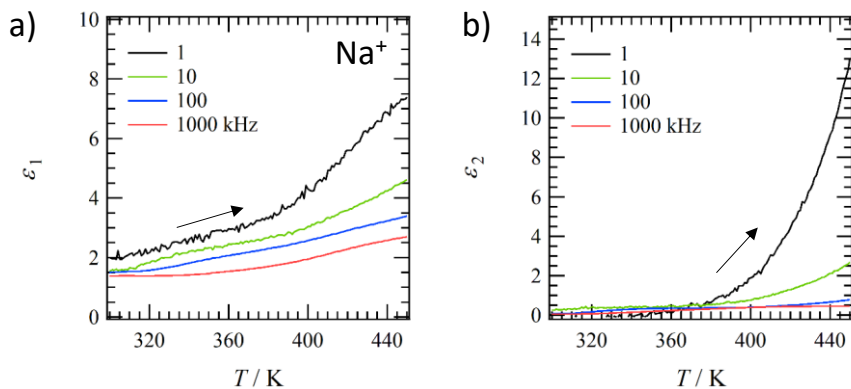


Figure S7. Temperature and frequency dependent real and imaginary parts of dielectric constants (ϵ_1 and ϵ_2) for pellet of unhydrated crystal **1'**.

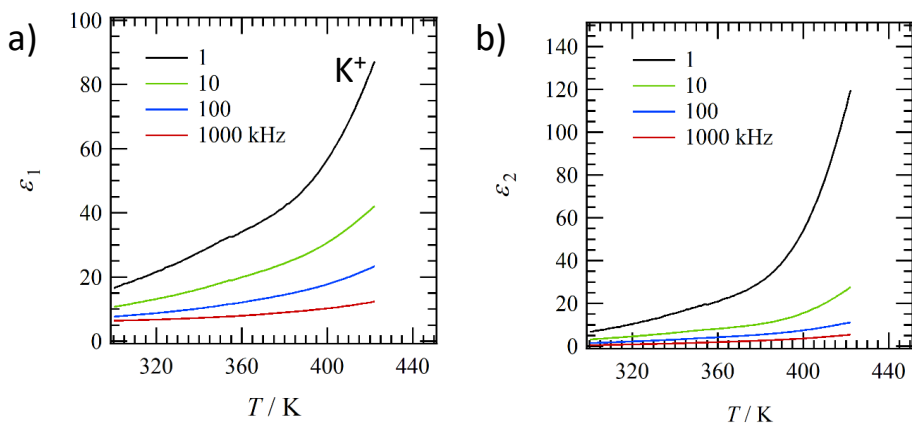


Figure S8. Temperature and frequency dependent real and imaginary parts of dielectric constants (ϵ_1 and ϵ_2) for pellet of crystal **2**.

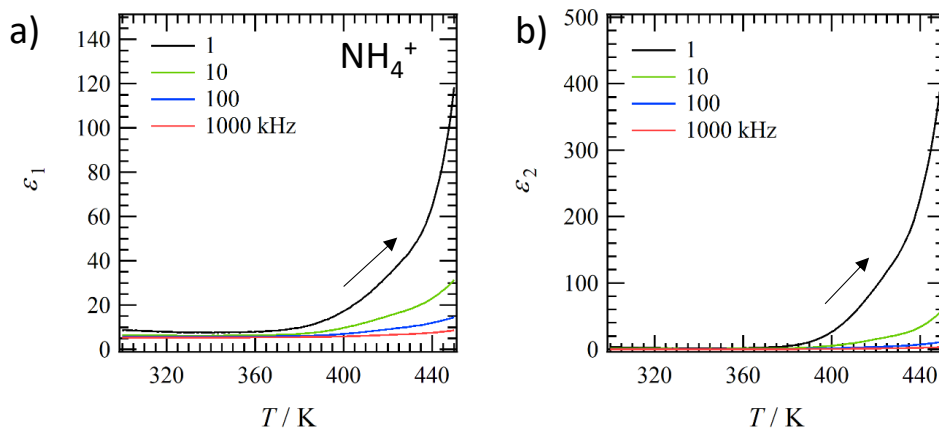


Figure S9. Temperature and frequency dependent real and imaginary parts of dielectric constants (ϵ_1 and ϵ_2) for pellet of crystal **3**.

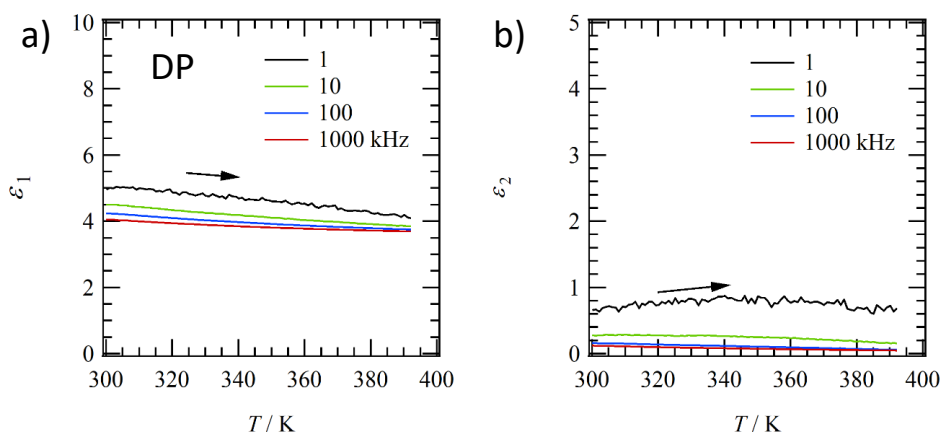


Figure S10. Temperature and frequency dependent real and imaginary parts of dielectric constants (ϵ_1 and ϵ_2) for pellet of crystal **4**.

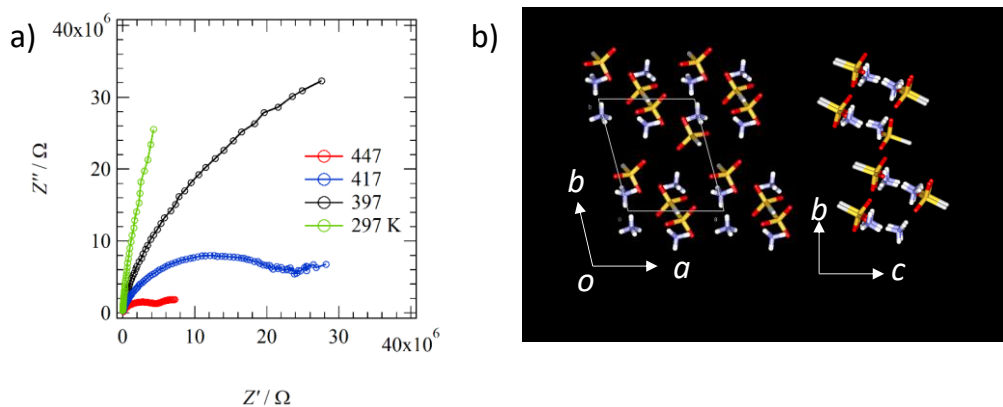


Figure S11. Proton conductivity of crystal **3** with temperature dependent Cole-Cole plots and proton transport layer.

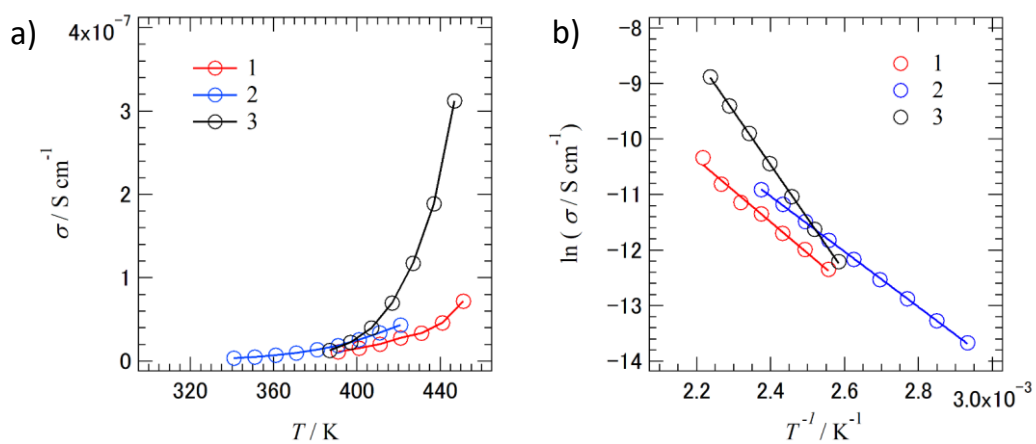


Figure S12. Temperature dependent ionic conductivities of crystals **1**, **2**, and **3**.

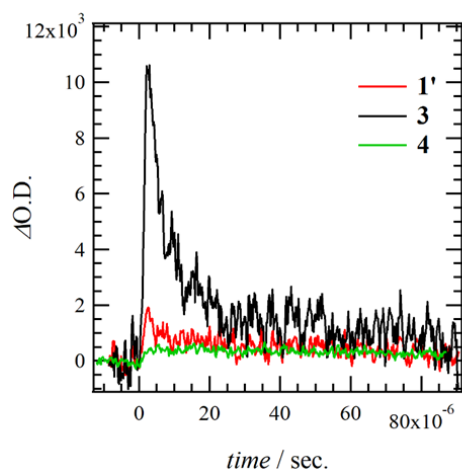


Figure S13. TAS spectra of thin films **1 – 4**.

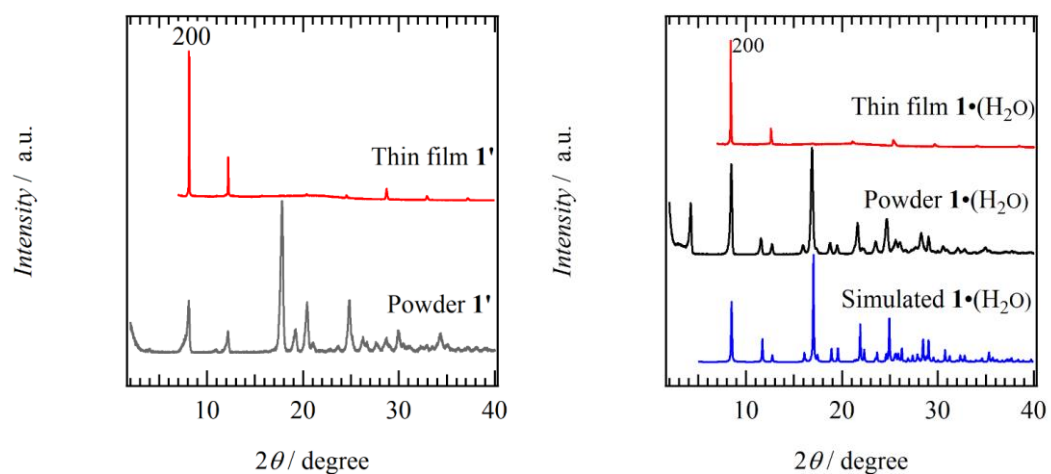


Figure S14. PXRD patterns of powder **1'**, thin film **1'**, and the simulation of **1** based on the single crystal X-ray analysis.

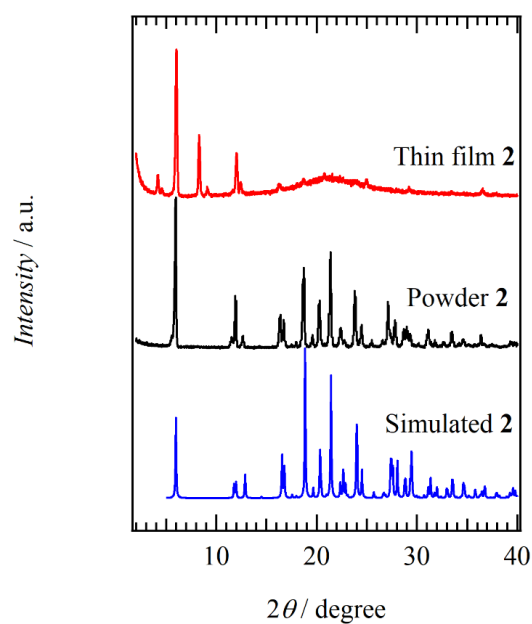


Figure S15. PXRD patterns of powder **2**, thin film **2**, and the simulation of **2** based on the single crystal X-ray analysis.

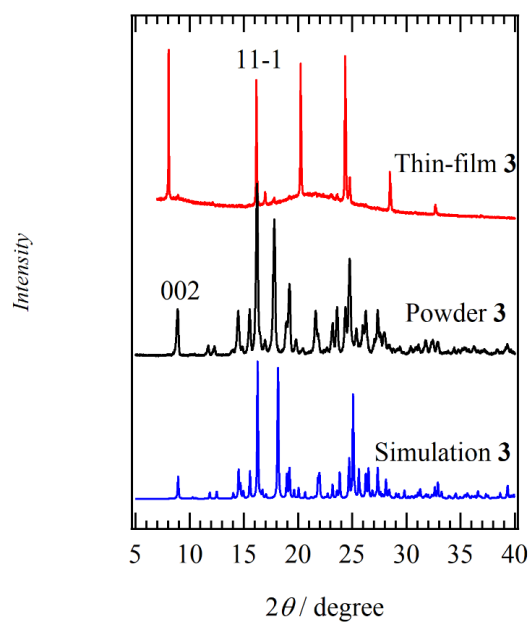


Figure S16. PXRD patterns of powder **3**, thin film **3**, and the simulation of **3** based on the single crystal X-ray analysis.

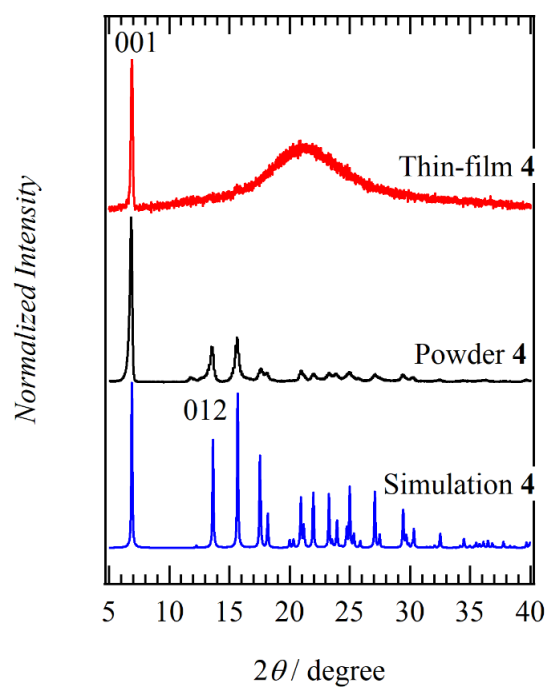


Figure S17. PXRD patterns of powder **4**, thin film **4**, and the simulation of **4** based on the single crystal X-ray analysis.

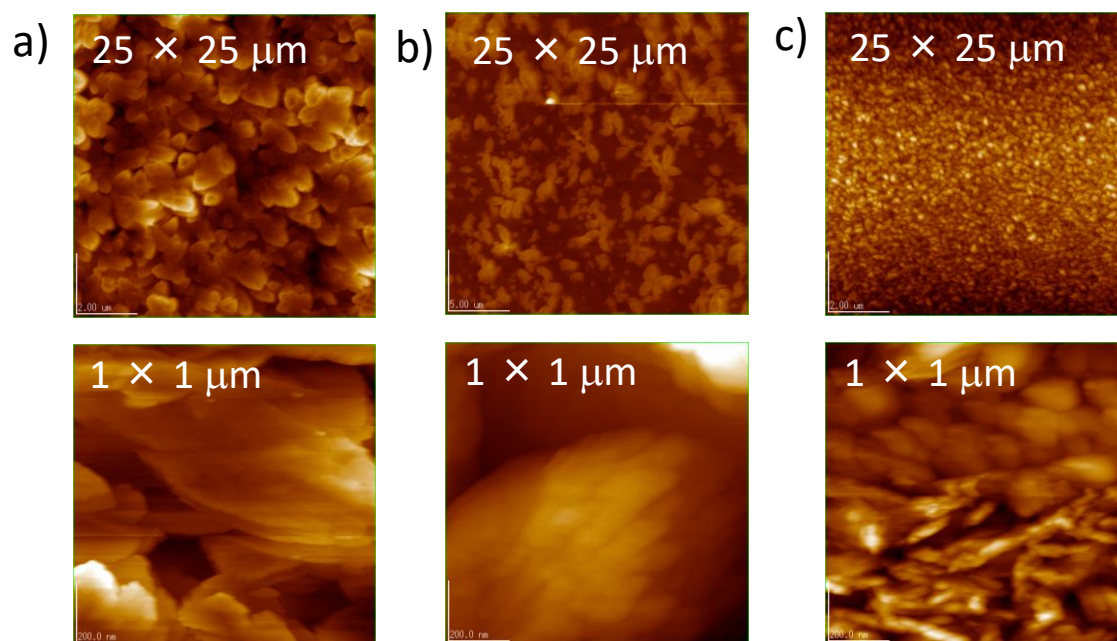


Figure S18. AFM images of thin films a) **1**, b) **2**, and c) **3** for the scanning range of $25 \times 25 \mu\text{m}^2$ (upper) and $1 \times 1 \mu\text{m}^2$ (lower).